Chemical Science

Accepted Manuscript

This article can be cited before page numbers have been issued, to do this please use: W. Luo, Q. Wang, X. Li, F. Zhang, Y. Fu, Y. Fu, X. Zhang, G. Zhang, X. Liu and J. Luo, *Chem. Sci.*, 2026, DOI: 10.1039/D6SC00286B.

ROYAL SOCIETY OF CHEMISTRY

rsc.li/chemical-science

View Article Online
DOI: 10.1039/D6SC00286B

ARTICLE

Dimensional Engineering in Chiral Layered Hybrid Perovskites for High-Anisotropy Self-powered Circularly Polarized Light Detection

Received 00th January 20xx,
Accepted 00th January 20xx

DOI: 10.1039/x0xx00000x

Wan Luo[a,b], Qianxi Wang[a], Xiaoqi Li[a], Fen Zhang[a], Yan Fu[a,b], Yikun Fu[a,b], Xiaoyu Zhang[a,b], Guifu Zhang[a], Xitao Liu[a,b,c*] and Junhua Luo[b,c]

Chiral perovskites have emerged as a highly promising family of materials for circularly polarized light (CPL) detection, owing to their unique combination of structural chirality and remarkable optoelectronic performance. However, breaking the linear scaling law between chiroptical activity and intrinsic conductivity with dimensionality remains a substantial challenge toward high-performance CPL detection. Herein, through dimensional engineering involving the incorporation of a large cage cation and a chiral bifunctional bulky cation, a series of chiral layered hybrid perovskites (*R/S*-BrBA)$_2$EA$_{n-1}$Pb$_n$Br$_{3n+1}$ (*n* = 1 to 3, *R/S*-BrBA$^+$ is 3-amino-1-bromobutanium and EA$^+$ is ethylammonium) has been successfully constructed. By incorporating oversized EA$^+$ within the layered perovskite lattices, two new pairs of mutilayered hybrid perovskites (*R/S*-BrBA)$_2$EAPb$_2$Br$_7$ (2*R/S*) and (*R/S*-BrBA)$_2$EA$_2$Pb$_3$Br$_{10}$ (3*R/S*) have been synthesized, which exhibit remarkable semiconducting properties including small optical absorption edges (2.79 and 2.69 eV) and high photoconductive on/off ratio (> 10^2 and 10^3). Strikingly, cooperatively driven by the large cation induced lattice expansion and bifunctional cation introduced halogen···halogen Interaction increases the chirality transfer from the organic to inorganic sublattices, and the chiroptical activity with an asymmetric factor was enhanced by 5.7 times as the *n* value increases, breaking the linear scaling law. Benefiting from the dimensional engineering, exceptional self-powered CPL detection with an anisotropy factor (g_{iph}) of up to 0.278 has been achieved in photoelectric device fabricated with 3*R* single crystals. This study provides a pathway for the development of chiral perovskites that integrate high chiroptical activity and remarkable intrinsic conductivity, thereby enabling high-anisotropy self-powered CPL detection.

Introduction

Circularly polarized light (CPL) detection, as a form of selectively responding to the intrinsic handedness of chiral light, is attracting increasing attention for its extensive utilization in diverse applications, including remote sensing, optical sensing, biological imaging, and many other fields.[1–4] Compared with conventional achiral substances, chiral semiconductors that possess intrinsic chiroptical anisotropy present a distinct advantage in the direct discrimination of CPL without the requirement for external optical components like polarizers or wave plates.[5,6] Particularly, the straightforward operation mode and high detection efficiency of chiral semiconductor devices provide a more efficient and convenient detection path for realizing CPL detection.[7,8] Since the chiroptical properties of chiral hybrid perovskites were unveiled, these extraordinary materials featuring a unique combination of structural chirality and remarkable optoelectronic performance have emerged as a fascinating family of chiral semiconductors for CPL detection.[9–16] For example, Chen et al. developed a chiral hybrid perovskite *R/S*-α-PEAPbI$_3$ (PEA$^+$ is phenylethylaminium) by incorporating a chiral cation into the perovskite lattice, which facilitated efficient direct CPL detection with a responsivity of 797 mA W^{-1}.[17] Despite their tunable band gaps, exceptional optical characteristics, and distinctive low-dimensional architectures, chiral hybrid perovskites still suffer from limited semiconducting properties.[18,19]

Over the past decade, substantial efforts have been devoted to exploring appropriate chiral hybrid perovskites with enhanced intrinsic conductivity for CPL detection through dimensional engineering.[20–24] Among them, chiral layered hybrid perovskites, specially those featuring multilayered architectures, have shown promising potential for CPL detection owing to due to their prominent semiconducting properties, including high carrier mobility, long carrier diffusion length, and suitable bandgaps.[15,25,26] As a result, a series of multilayered chiral perovskites have been successfully developed, such as (*R/S*-MPEA)$_2$MA$_{n-1}$Pb$_n$I$_{3n+1}$ (*n* = 1 to 3, MPEA$^+$ is methylphenylethylammonium, MA$^+$ is methylammonium), (*R/S*-NEA)$_2$(MA)$_2$Pb$_3$I$_{10}$ (NEA$^+$ is naphthylethylammonium).[13,27] However, despite remarkable advancements in intrinsic conductivity achieved through increasing the inorganic sublattice layer number (*n*), this enhancement often comes at the expense of a diminished chiroptical response and a reduced dissymmetry factor, impairing the sensitivity and efficacy of CPL detection.[28,29] Therefore, overcoming the linear scaling law between

[a] State Key Laboratory of Functional Crystals and Devices, Fujian Institute of Research on the Structure of Matter, Chinese Academy of Sciences Fuzhou, Fujian 350002, China.
[b] College of Chemistry and Materials Science, Fujian Normal University, Fuzhou, Fujian 350007, P.R. China University of Chinese Academy of Sciences, Beijing 100049, China.
[c] Fujian College, University of Chinese Academy of Sciences, Fuzhou, Fujian 350002, P.R. China

† Supplementary Information available: [details of any supplementary information available should be included here]. See DOI: 10.1039/x0xx00000x

chiroptical activity and conductivity, which dictates that an increase in dimensionality leads to higher conductivity but lower chiroptical activity, remains a challenging task in multilayered chiral perovskites[30–36]. It is well established that non-covalent interactions, including hydrogen bonding, π–π stacking, and halogen···halogen bonding, play a significant role in chiral transfer between the inorganic sublattice and the chiral organic sublattice.[37,38] For example, Jooho Moon and others enhanced the chirality transfer by inducing inorganic framework distortion via the introduction of intermolecular halogen···halogen bondings.[39] Meanwhile, oversized organic cations, such as ethylammonium (EA^+), dimethylammonium (DMA^+), and guanidinium (GA^+) with larger radii are expected to enhance the lattice distortion and generate large symmetry breaking and chirality.[40] Inspired by these results, through incorporation of bifunctional bulky cations with non-covalent interactions in multilayered chiral perovskites is expected to provide an exciting pathway to develop appropriate chiral hybrid perovskites for CPL detection.

Herein, we designed a series of chiral layered perovskites $(R/S\text{-BrBA})_2EA_{n-1}Pb_nBr_{3n+1}$ (n = 1 to 3, R/S-$BrBA^+$ is 3-amino-1-bromobutanium). Chiroptical activity measurements revealed that this series of materials breaks the scaling law where chiral optical activity linearly decreases with increasing perovskite layer number. The Circular dichroism (CD) signal for $(R/S\text{-BrBA})_2EA_2Pb_3Br_{10}$ (3R/S) is 5.7 times higher than that of bilayered counterpart $(R/S\text{-BrBA})_2EAPb_2Br_7$ (2R/S). This phenomenon arises from the distortion index of the outermost inorganic framework, generating stronger local electric field gradients. Benefiting from enhanced semiconductor properties and chiroptical activity, exceptional self-powered CPL detection with an anisotropy factor up to 0.278 has been achieved in a device fabricated with 3R single crystals, validating a pathway for the development of multilayered chiral perovskites in CPL sensing.

Results and discussion

Multilayered perovskite architectures exhibit exceptionally efficient carrier transport, owing to synergistic band alignment and reduced interfacial recombination.[41,42] The inset in Fig. 1 shows the tolerance factors for the interlayer cations commonly used in constructing multilayer perovskite. Current research predominantly focuses on chiral perovskites incorporating conventional small cations such as MA^+, formamidinium (FA^+), and cesium (Cs^+).[43,44] Herein, we synthesized the chiral monolayered perovskite $(R/S\text{-BrBA})_2PbBr_4$ (1R/S) via a bifunctional chiral cation R/S-BrBA.[45,46] To obtain multilayer perovskites with enhanced semiconducting properties, we tuned the number of structural layers and their optical activity, and further introduced EA as a spacer cation, successfully constructing the quasi-two-dimensional structure 2R/S.

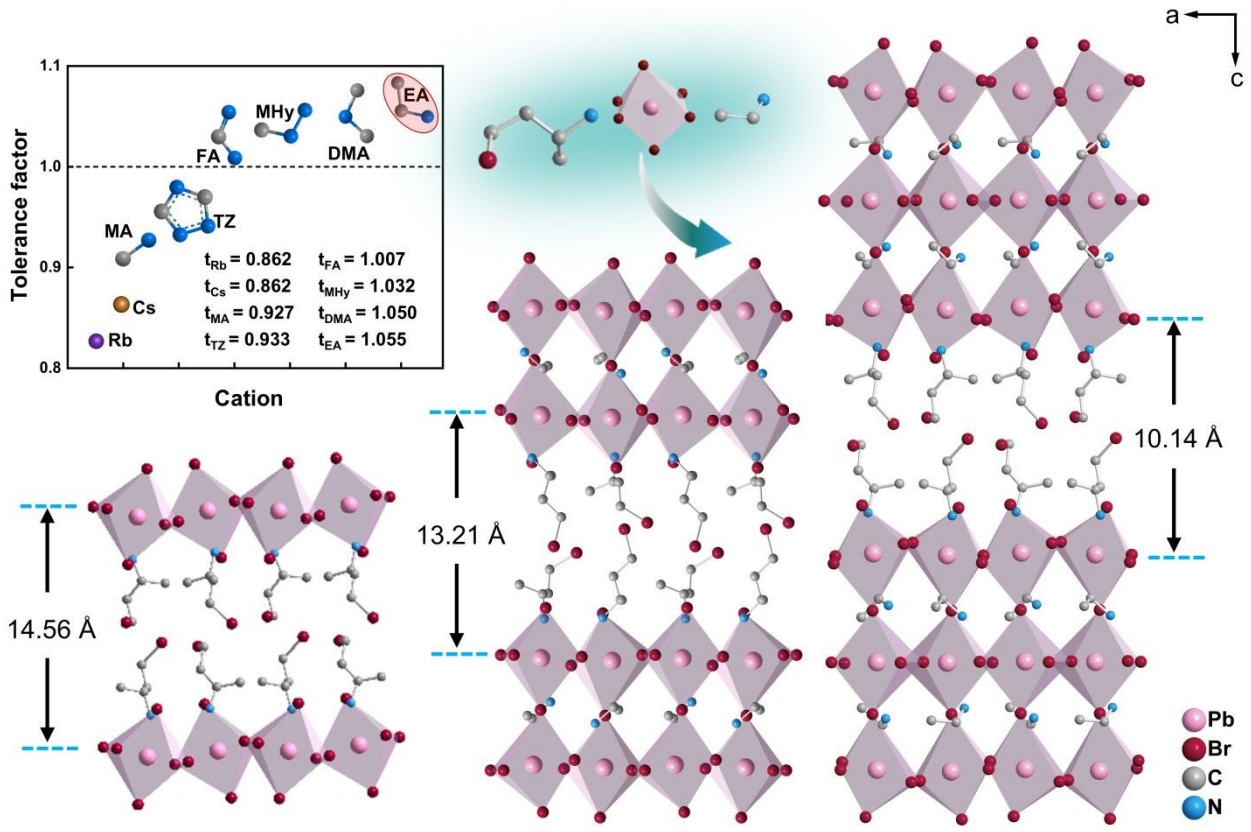

Fig. 1 Bromo-(*R*)-3-amino-1-butanol and lead bromide octahedra form $(R\text{-BrBA})_2PbBr_4$. (1R), which subsequently reacts with EA (ethylamine) to yield $(R\text{-BrBA})_2EAPb_2Br_7$ (2R)and $(R\text{-BrBA})_2EA_2Pb_3Br_{10}$ (3R). (MA denotes methylammonium, FA denotes formamidinium, MHy denotes methylhydrazinium, TZ denotes 1,2,4-Triazole, DMA denotes dimethylamine.) Corresponding hydrogen atoms of organic cations are omitted for clarity. H atoms are omitted for clarity.

View Article Online
DOI: 10.1039/D6SC00286B

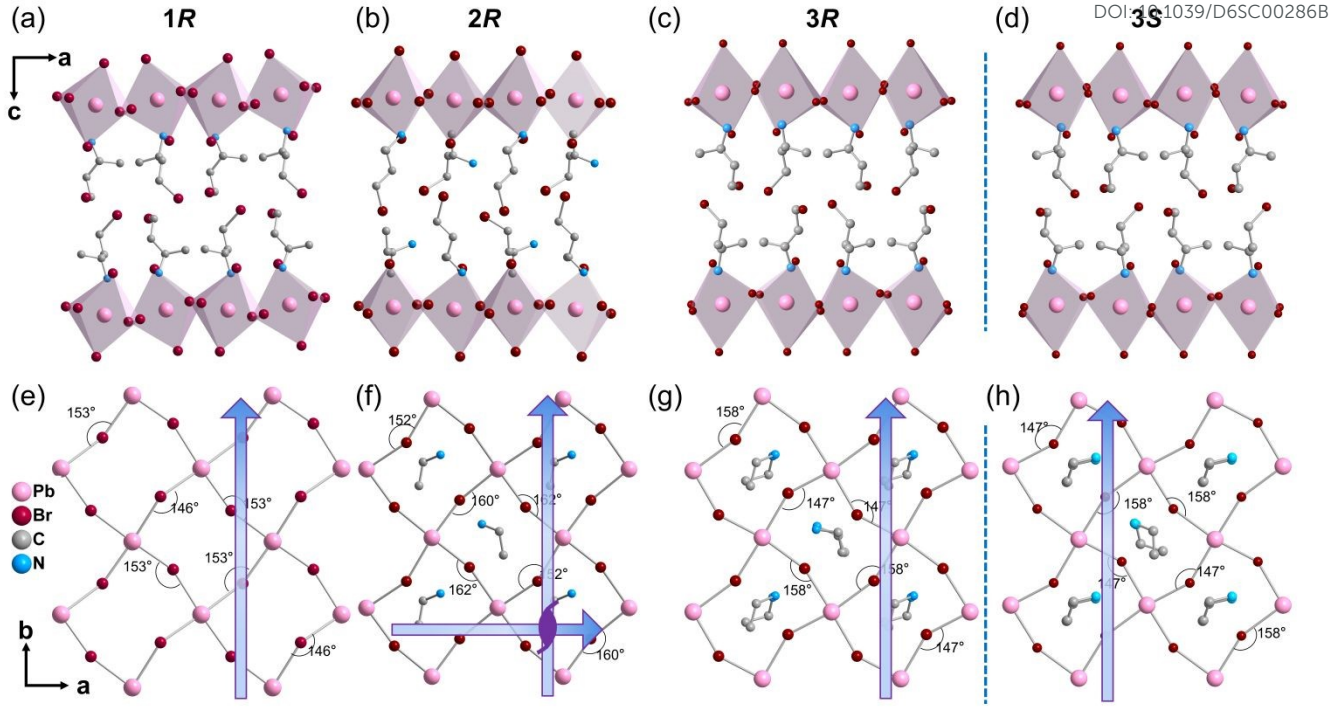

Fig. 2 Organic-inorganic interface coupling structures of 1*R*, 2*R*, and 3*R/S*. (a) 1*R*. (b)2*R*. (c) 3*R*. (d) 3*S*. Side-view crystal structures of 1*R*, 2*R*, and 3*R/S* along the c-axis. (e) 1*R*. (f) 2*R*. (g) 3*R*. (h) 3*S*. The blue arrows represent the three mutually perpendicular 2_1 helix axes of 2*R/S* and the single 2_1 helix axis of 3*R/S* parallel to the *b*-axis. The blue dashed line represents the mirror image. H atoms are omitted for clarity.

Structural characterization revealed that 2*R/S* exhibits significantly reduced octahedral distortion between layers compared with 1*R/S*, which directly leads to a weaker CD signal. Subsequently, by precisely adjusting the stoichiometric ratio of lead acetate to EA^+, we ultimately obtained chiral trilayered perovskites 3*R/S* with enhanced interfacial octahedral distortion, whose chiroptical response is markedly stronger than that of the 2*R/S* (Fig. 1). Bulk 3*R/S* single crystals with dimensions of 3 × 3 × 0.5 mm^3 were successfully prepared by oriented insertion of bromine-substituted chiral *R/S*-BrBA cations into the $[PbBr_6]^{4-}$ inorganic backbone using a controlled cooling process (Fig. S1). The constructed 1*R/S*, 2*R/S*, and 3*R/S* structures are Ruddlesden-Popper type hybrid perovskites with the chemical formula $(R\text{-}NH_3)_2A_{n-1}M_nX_{3n+1}$ (*R*-NH_3: organic spacer cation; A: a small cation in the inorganic framework; M: metal cation; X: halide ion; *n*: layer number), which consists of alternating layers of organic cations and inorganic framework.[47] Powder X-ray diffraction (XRD) patterns confirmed the phase purity of 1*R/S*, 2*R/S*, and 3*R/S* (Fig. S2). Single crystal structures of 2*R/S* and 3*R/S* were collected. Further analysis through structural refinement confirmed the high phase purity and thermal stability of 3*R/S*, with a decomposition temperature reaching 513 K (Fig. S3). X-ray crystallography analysis indicates that 2*R/S* crystallizes in a space group $P2_12_12_1$, while the 1*R/S* and 3*R/S* compounds crystallize in polar space group $P2_1$. Structural analysis reveals an intriguing trend in octahedral distortion at the organic-inorganic interface that as the number of perovskite layers increases from *n* = 1 to *n* = 2, the degree of octahedral distortion decreases. However, when the layer number further increases to *n* = 3, the distortion of the interface octahedra actually increases. This distortion manifests as fluctuations in the Pb–Br bond length ranging from 2.817 to 3.29 Å and in the Br–Pb–Br bond angle ranging from 78.35° to 177.98° (Tables S1–S14). The average bond angle of the Pb–Br–Pb bond in the 1*R* structure is 149.5°, while it is 159° in the 2*R* structure and 152.8° in the 3*R* structure. The Pb–Br–Pb bond network in 3*R* exhibits helical distortion, resulting in greater spatial asymmetry, which may lead to enhanced chirality transfer. (Fig. 2). This enhanced distortion reduces Br···Br distances (Fig. S4), thereby significantly strengthening halogen bonding interactions, and the organic and inorganic layers were spatially arranged alternately, resulting in the construction of a natural quantum well structure. When the chiral perovskite transitions from *n* = 1 to *n* = 3, its interlayer spacing decreases from 14.56 Å to 10.14 Å (Fig. 1). The smaller interlayer spacing enhances electronic coupling between adjacent layers, thereby improving electron mobility and photovoltaic conversion efficiency.[48] Additionally, the reduced interlayer spacing strengthens interlayer forces, such as van der Waals forces and hydrogen bonds, which help to enhance the material's thermal stability.[49]

View Article Online
DOI: 10.1039/D6SC00286B

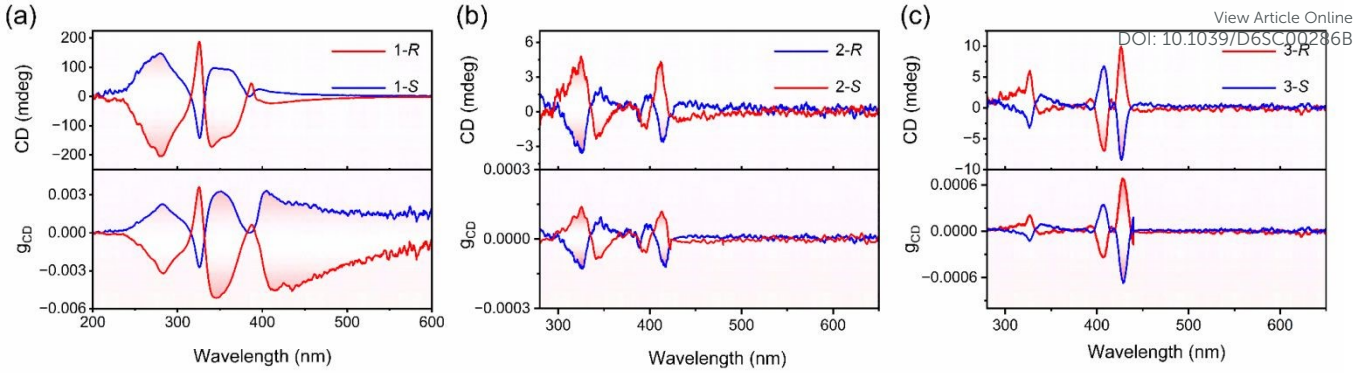

Fig. 3 (a) Circular dichroism (CD) and g_{CD} spectra of 1*R* and 1*S* films. (b) CD and g_{CD} spectra of 2*R* and 2*S* films. (c) CD and g_{CD} spectra of 3*R* and 3*S* films.

Two fundamental prerequisites serve as crucial elements for achieving highly sensitive CPL detection, significant chiral light absorption, and outstanding semiconductor performance. Table 15 presents some research data on the dimensionality, chiroptical activity, and conductivity of chiral perovskites. The optical properties of perovskites were evaluated using CD spectroscopy. As with other reported 2D chiral hybrid perovskites, CD signals of opposite signs are observed between 1*R* and 1*S*, 2*R* and 2*S*, and between 3*R* and 3*S* near exciton absorption and interband transitions, respectively. [23,50,51] The CD spectrum of 1*R/S* exhibits distinct peaks with opposite signs at 325 nm and 356 nm. The CD spectrum of 2*R/S* shows distinct peaks with opposite signs at 395 nm and 413 nm. In contrast, the CD signals of 3*R/S* are located at 407 nm and 430 nm, respectively, and exhibit opposite signs at the corresponding wavelengths (Fig. 3a-c, Fig. S5). These distinct CD signals arise from the chiral-induced splitting of the degenerate energy states of the inorganic framework, modulated by the chiral organic cations. From the CD spectra, the dimensionless anisotropy factor (g_{CD}) was extracted using the equation.

$$g_{\mathrm{CD}} = \frac{\mathrm{CD\ (mdeg)}}{32980 \times \mathrm{absorbance}}$$

The g_{CD} of the 1*R/S* film at 325 nm is 3.3×10^{-3}, the g_{CD} of the 2*R/S* film at 413 nm is 1.18×10^{-4}, while the g_{CD} of the 3*R/S* film at 430 nm reaches 6.83×10^{-4} (Fig. 3a-c). It is noteworthy that when the structure transitions from $n = 2$ to $n = 3$ configuration, the chirality typically weakens.[28] However, the g_{CD} of 3*R/S* is larger than that of 2*R/S*. This is because the chirality transfer efficiency of perovskites correlates with the degree of distortion in the inorganic framework.[52,53] Calculations in this study indicate that the interfacial octahedra directly coordinated to the organic layer in 3*R/S* exhibit greater distortion. A distortion of $[PbBr_6]^{4-}$ octahedron was quantitatively evaluated by the octahedral band-length variance of Δd

$$\Delta d = \frac{1}{6}\sum_{i=1}^{6}\left[\frac{d_i - d}{d}\right]^2$$

(Where d_i denotes each individual Pb–Br bond length and d represents the mean Pb–Br distance within the $[PbBr_6]^{4-}$ octahedron.) The calculated Δd was 0.0023 for 3*R*, which is larger than Δd is 0.0017 for 2*R* (Fig. S6). The Pb–Br bond length distortion in 3*R*, combined with the helical distortion of the Pb–Br–Pb bond angle network observed in our structure, further disrupts the structural center symmetry and enhances chiral transfer. Quantitative analysis of Hirshfeld surfaces revealed that 3*R* exhibits stronger intermolecular forces, with the proportion of N–H Br hydrogen bonds increasing from 27.7% in 2R to 43% in 3*R*, accompanied by shorter hydrogen bond lengths (2.49 Å and 2.65 Å for 3*R*, compared to 2.54 Å and 2.62 Å for 2*R*). Additionally, the proportion of Br Br halogen bonds rose from 0.7% in 2*R* to 2.3% in 3*R*, further enhancing interlayer lattice strain transfer at the organic-inorganic interface through intercalated halogen bridges that strengthen interlayer electronic coupling. The enhanced hydrogen bond anchoring and directional halogen bonding interactions collectively improve the chiral transfer efficiency between organic cations and inorganic frameworks (Fig. S7).[37,54–57] Meanwhile, the EA^+ cations of the larger lattice make the inorganic backbone octahedral asymmetry increase, leading to stronger chiral transfer between the inorganic and organic layers in the trilayer structure, with the g_{CD} of the perovskite of 3*R/S* being ~5.7 times larger than that of 2*R/S*. This finding not only enriches our understanding of chiral perovskite materials but also provides new ideas for designing and optimizing materials with specific chiral optical properties.

Furthermore, the reduced interlayer distance enhances electronic coupling across the inorganic layers, resulting in a narrow bandgap and consequently improved light absorption, which are beneficial semiconducting characteristics. The application of 2D hybrid perovskites in optoelectronic devices is influenced by their semiconductor and optical properties. Therefore, we further conducted ultraviolet-visible absorption and photoluminescence (PL) measurements to investigate their related properties. As shown in Fig. 4a, the UV-vis absorption spectra of 1R, 2R and 3R have obvious absorption cutoffs at 427 nm, 452 nm and 469 nm, respectively. The corresponding optical band gaps for 1*R*, 2*R*,

View Article Online
DOI: 10.1039/D6SC00286B

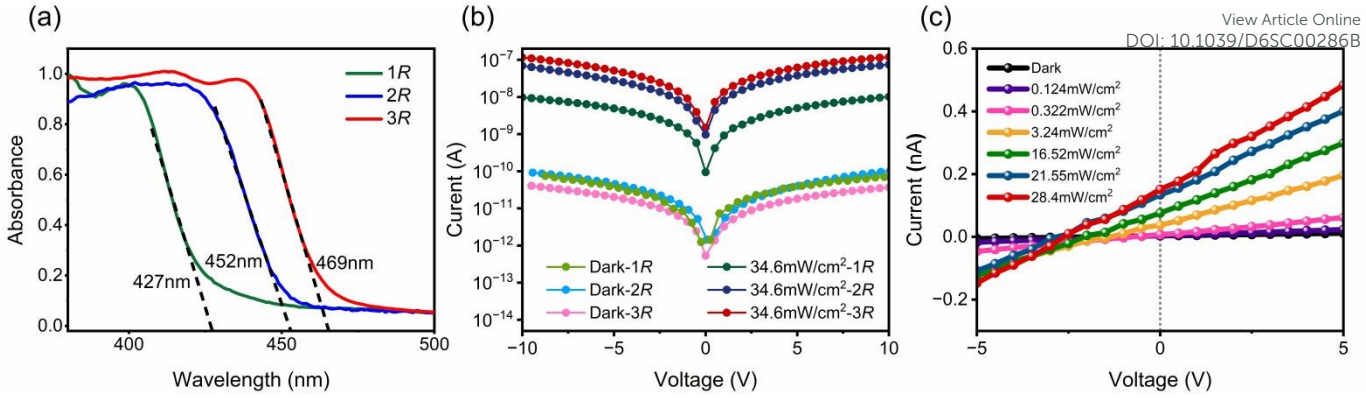

Fig. 4 (a) Ultraviolet absorption spectra of 1*R*, 2*R* and 3*R*. (b)Dark-current and photocurrent curves of 1*R*, 2*R,* and 3*R* measured at 405 nm illumination (photocurrent recorded under 34.6 mW cm^{-2}). (c) Photovoltage measured along the b-axis versus optical current density of 3*R*.

and 3*R* were estimated from Tauc plots.[58] Fig. S8 shows that the optical bandgap of 1*R* is 3.02 eV, while the optical bandgap of 2*R* and 3*R* are 2.79 eV and 2.69 eV, respectively. Their density functional theory calculated structures indicate that they are all direct-bandgap semiconductors. Taking 3*R* as an example to analyze the origin of their optical properties, the partial density of states profiles show that the valence band maximum is mainly from the Br-4p orbitals, while the conduction band minimum is mainly contributed by the Pb-6p states (Fig. S9-11). These results suggest that the inorganic composition mainly determines the energy band structure of the chiral halide perovskites 3*R/S*. Furthermore, the photoluminescence spectra of 1*R*, 2*R* and 3*R* exhibit emission peaks at 462 nm, 464 nm and 469 nm, respectively, under 369 nm excitation. In addition, 1*R* shows a sub-bandgap emission peak at 590 nm and 2*R* at 530 nm. We attribute these peaks to self-trapped excitons (Fig. S12).[59–61] A photodetector based on large single crystals of 1*R*, 2*R,* and 3*R* at an optical power of 34.6 mW cm^{-2} was observed to have a larger photocurrent response for 3*R* than for 2*R* and 1*R*, and a current switching ratio of 10^3 was achieved for 3*R* (Fig. 4b). The responsivity (*R*) and detection (*D**) of 3*R* device were 0.36 A/mW and 1.21× 10^{13} Jones respectively (Fig.S13). The stability of hybrid perovskites significantly impacts their applications, including thermal stability and photocurrent reproducibility. As already mentioned, 3*R* has excellent thermal stability. Fig. S14 demonstrates that the powder XRD pattern of the crystals, which were stored for 30 days, is consistent with the powder XRD pattern of the freshly prepared crystals, indicating that 3*R* exhibits good phase stability. In addition, the stability of the 3*R*-based planar arrays was further investigated by comparing the I-V curves of fresh samples with those of samples that had been left for 30 days. After 30 days of air exposure, the dark currents and photocurrents of the samples remained consistent with those of fresh devices (Fig. S15), and the photocurrent performance of the 3*R* did not degrade after several cyclic switching tests (Fig. S16), further demonstrating the robust reproducibility of crystal device photocurrents. Moreover, 3*R* was found to exhibit an intrinsic bulk photovoltaic effect under zero external bias, delivering a photovoltage of 2.2 V along the *b*-axis (Fig. 4c and S17). Notably, this photovoltage exceeds values previously reported for layered hybrid perovskites, including $(C_4H_9NH_3)_2(NH_2CHNH_2)Pb_2Br_7$ (0.4 V)[62], $(CH_3OC_3H_9N)_2CsPb_2Br_7$ (0.5 V)[29], $EA_4Pb_3Br_{10}$ (0.5 V)[63], $(CPA)_2FAPb_2Br_7$ (0.25 V)[64]. This phenomenon suggests the existence of an inherent electric field and demonstrates that 3*R* is capable of detecting photons in a self-powered mode without requiring external bias. Conversely, the photovoltages along the *a*- and *c*-axes are nearly undetectable. The fact that photovoltage is observed only along the *b*-axis further validates that the photovoltaic effect is due to the chiral-polar nature.

To evaluate the inherent CPL detection capability of the 3*R*, Fig. 5a and Fig. S18 schematically depicts a planar single-crystal device with Ag electrodes fabricated within the *ab* plane. That is, carriers will be transported along the *b*-axis of the polarization direction, leading to the chiral-polar photovoltaic effect when illuminated by CPL. This setup paves the way for further self-powered CPL detection. The device is illuminated with 405 nm polarized light, whose handedness is precisely controlled by a quarter-wave plate. As shown in Fig.5b, under the same intensity of laser irradiation, the photocurrent of right-handed (RCP) is much larger than that of left-handed (LCP), revealing a significant differentiation ability under RCP and LCP lasers (V_{bias} = 0 V). Meanwhile, the photocurrent remained almost constant under multiple CPL cycles (Fig. 5c). The device was confirmed to be stable and suitable for detecting CPL. Therefore, the discrimination between RCP and LCP was quantified via the photocurrent anisotropy factor g_{Iph}, which was derived from the equation.

$$g_{\mathrm{Iph}} = 2\frac{I_{\mathrm{ph}}^{\mathrm{R}} - I_{\mathrm{ph}}^{L}}{I_{\mathrm{ph}}^{\mathrm{R}} + I_{\mathrm{ph}}^{L}}$$

Where $\boldsymbol{I}_{ph}^{R}$ and $\boldsymbol{I}^{\boldsymbol{bh}}$ denote the photocurrents under RCP and LCP irradiation. A g_{Iph} value of 0.278 was determined, which is an outstanding figure in multilayer chiral perovskite materials, even surpassing the current reported levels of chiral perovskite direct CPL detectors based on such semiconductor materials, such as $[(R)\text{-}\beta\text{-MPA}]_2MAPb_2I_7$ (0.2)[10], $(R\text{-}\alpha\text{-PEA})_2PbI_4$ (0.23)[17], $(R/S\text{-MPA})_2PbCl_4$ (0.1)[65], and others.[13,39,66–69] Some of the reported experimental g_{Iph} for layered CPL detectors are summarized in Table S16 and Fig. 5f. As shown

View Article Online
DOI: 10.1039/D6SC00286B

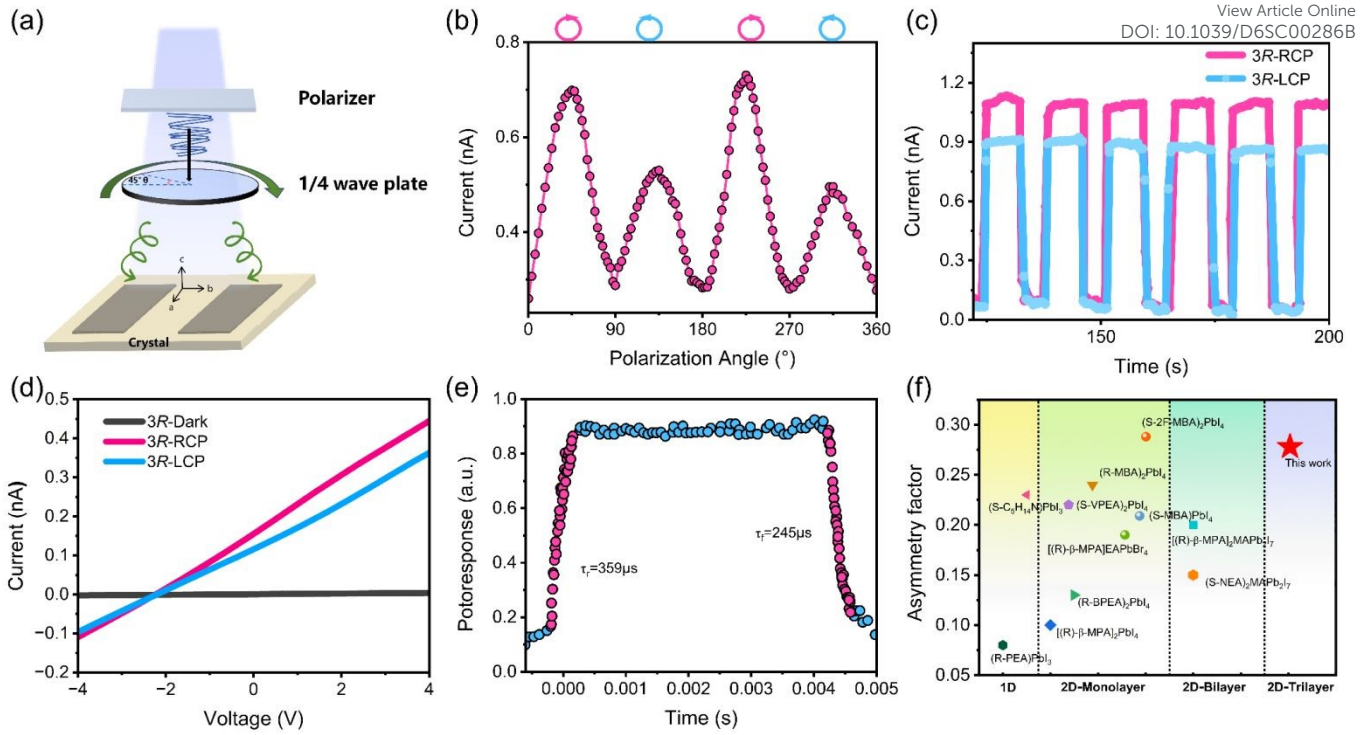

Fig. 5 (a) Schematic diagram for circular polarized light detection (CPL). (b) Photocurrent of the 3*R* device as a function of the rotation angle of the quarter-wave plate. (c) Photocurrent switching under alternating right-handed (RCP) and left-handed (LCP) illumination of the device under 405 nm light illumination with the intensity at 28.4mW cm^{-2}, 0 V_{bias}. (d) I–V characteristics along the b-axis of the 3R device measured in the dark, under LCP-405 nm illumination, and under RCP-405 nm illumination. (e) The response time of the 3*R* detector during the light-on/off switching. (f) Summarizing the asymmetry factors of some reported CPL detectors.

in Fig. 5d, the photocurrent varies with the excitation of RCP or LCP light, and there is still a 2.2 V bulk photovoltaic effect under RCP and LCP light. Under RCP light illumination at 10 V, the rise and decay times of the measurements were about 359 and 245 μs, respectively (Fig. 5e). This rapid response highlights the potential of 3R for use in high-speed detection systems. These benefits allow well-engineered chiral polarized hybrid perovskite materials to exhibit significant promise in the realm of self-powered intelligent CPL detection.

Conclusions

In summary, this work systematically investigates the structure-property relationships in chiral perovskite single crystals, revealing that the trilayer (3*R*) configuration exhibits superior optoelectronic performance compared to monolayer (1*R*) and bilayer (2*R*) counterparts. The 3*R* perovskite demonstrates remarkable photodetection capabilities with a current switching ratio of 10^3 and a significant bulk photovoltaic effect, generating 2.2 V photovoltage along the *b*-axis. These properties stem from the unique structural characteristics of 3*R*, where interfacial octahedral distortion (0.0023 vs 0.0017 for 2*R*) and enhanced electronic coupling through halogen bridges facilitate efficient charge separation and transport. Furthermore, the material shows exceptional chiral optical properties with an anisotropy factor g_{CD} of 6.83 × 10^{-4} at 430 nm, which is 5.7 times higher than that of 2*R*, enabling sensitive CPL detection. The fabricated self-powered CPL detector achieves an outstanding photocurrent anisotropy factor g_{Iph} of 0.278 with fast response times (rise/decay: 359/245 μs), outperforming existing chiral perovskite-based detectors. This work not only offers a new route for designing chiral perovskites but also shows their potential in making high-performance, self-powered optoelectronic devices. It also broadens the possibilities of multilayer chiral perovskites in self-powered CPL detection.

Experimental

Materials

Synthesis of (*R/S*-BrBA)$_2$PbBr$_4$. Dissolve lead(II) acetate trihydrate (0.76 g, 2 mmol) in 10 mL of HBr. Subsequently, (*R/S*)-3-amino-1-butanol (0.36 g, 4 mmol) is added to this clear solution, and proceeded with heating, stirring, and volatilization for a period of time. When the hot solution is cooled to room temperature, (*R/S*-BrBA)$_2$PbBr$_4$ microcrystals are obtained. By reducing the temperature from 303 K to 283 K at a cooling rate of 0.5 K day^{-1}, high-quality (*R/S*-BrBA)$_2$PbBr$_4$ single crystals are grown.

Synthesis of (*R/S*-BrBA)$_2$EAPb$_2$Br$_7$. Dissolve lead(II) acetate trihydrate (0.76 g, 2 mmol) in 10 mL of HBr. Subsequently, add (*R/S*)-3-amino-1-butanol (0.36 g, 4 mmol) to the clear solution, and proceed with heating, stirring, and volatilization for a

period of time. (*R/S*-BrBA)$_2$PbBr$_4$ microcrystals are obtained when the hot solution cools to room temperature. Then, add ethylamine (0.045 g, 1 mmol), lead(II) acetate trihydrate (0.76 g, 2 mmol), and heat with stirring until the solution becomes clear. After standing to cool, (*R/S*-BrBA)$_2$EAPb$_2$Br$_7$ crystals are obtained. High-quality (*R/S*-BrBA)$_2$EAPb$_2$Br$_7$ single crystals are grown by reducing the temperature from 303 K to 283 K at a cooling rate of 0.5 K day^{-1}.

Synthesis of (*R/S*-BrBA)$_2$EA$_2$Pb$_3$Br$_{10}$. Dissolve lead(II) acetate trihydrate (0.76 g, 2 mmol) in 10 mL of HBr. Subsequently, add (*R*)/(*S*)-3-amino-1-butanol (0.36 g, 4 mmol) to the clear solution, and proceed with heating, stirring, and volatilization for a period of time. (*R/S*-BrBA)$_2$PbBr$_4$ microcrystals are obtained when the hot solution cools to room temperature. Then, add ethylamine (0.09 g, 2 mmol), lead(II) acetate trihydrate (1.52 g, 4 mmol), and heat with stirring until the solution becomes clear. After standing to cool, (*R/S*-BrBA)$_2$EA$_2$Pb$_3$Br$_{10}$ crystals are obtained. High-quality (*R/S*-BrBA)$_2$EA$_2$Pb$_3$Br$_{10}$ single crystals were grown by slowly cooling from 303 K to 283 K at 0.5 K day^{-1}.

Material characterization and theoretical analysis

Powder XRD data were recorded on a Rigaku Miniflex 600 diffractometer (Cu Kα, 2ϑ = 5 – 40°, 0.5° min^{-1}). Single-crystal XRD was collected on a SuperNova diffractometer (Mo Kα) and a Bruker D8 diffractometer (Mo Kα). The collected crystal data were refined using Olex2 software based on the F^2 full matrix method to obtain the crystal structure. Optical Bandgap were collected at room temperature using a PerkinElmer Lambda-950 spectrophotometer with a spectral scan from 280 to 650 nm at room temperature. CD measurement samples were fabricated on quartz substrates via spin coating. Pre-dried 1*R/S*, 2*R/S*, and 3*R/S* crystals were ground into powder and separately dispersed in anhydrous DMF, and the reaction was conducted in a glove box purged with nitrogen. The resulting precursor solution was spin-coated onto cleaned quartz substrates and annealed on a hot plate, yielding square samples. Measurements were subsequently performed at room temperature using a Jasco J-1500 circular dichroism spectrometer. Photoelectric measurements were performed using planar electrodes. Two symmetrical silver electrodes were sputtered on a single crystal plane with dimensions of 1.0 × 1.0 × 0.3 mm³. The distance between the electrodes was ~0.6 mm, and the thickness was ~0.05 mm. I-V curves and I-t curves were measured using a Keithley 6517B electrometer. Under a 405 nm laser beam (THORLABS, LP405-MF300), pure RCP and LCP were obtained by rotating the angle of the quarter-wave plate (from 45 to 135°), respectively. The response times were measured by a high-speed oscilloscope (Tektronix MDO3014) at a 10 V_{bias} voltage.

Supporting information

Supporting information associated with this article can be found in the online version.

Conflicts of interest

There are no conflicts to declare.

Acknowledgements

This work was supported by the National Natural Science Foundation of china (52473283, 22193042, 22125110, 22435005), the Strategic Priority Research Program of the Chinese Academy of Sciences (XDB1170000) the Self-deployed Key Project of State Key Laboratory of Functional Crystals and Devices(GNJT-2025-ZD01), the Natura Science Foundation of Fujian Province (2024J010037), and the Self-deployment Project Research Program of Haixi Institutes, Chinese Academy of Sciences(CXZX-2023-JQ04)

References

1 Y. Yang, R. C. Da Costa, M. J. Fuchter and A. J. Campbell, *Nat. Photonics*, 2013, **7**, 634–638.

2 Y. Dang, X. Liu, B. Cao and X. Tao, *Matter*, 2021, **4**, 794–820.

3 L. Xu, X. Wang, W. Wang, M. Sun, W. J. Choi, J.-Y. Kim, C. Hao, S. Li, A. Qu, M. Lu, X. Wu, F. M. Colombari, W. R. Gomes, A. L. Blanco, A. F. De Moura, X. Guo, H. Kuang, N. A. Kotov and C. Xu, *Nature*, 2022, **601**, 366–373.

4 Z. Xie, J. Deng, D. Liu, J. Lin, T. Jiang, X. Wang, W. Liu, L. Ma, F. Song, Z. Xiong, J. Chen, J. Zhang, C. Redshaw, Z. Zhao, X. Feng and B. Z. Tang, *Chem. Sci.*, 2026, DOI:10.1039.D5SC08358C.

5 F. J. Rodríguez-Fortuño, N. Engheta, A. Martínez and A. V. Zayats, *Nat. Commun.*, 2015, **6**, 8799.

6 J. Schmidt, A. Guggenmos, M. Hofstetter, S. H. Chew and U. Kleineberg, *Opt. Express*, 2015, **23**, 33564.

7 Z. Zhang, J. Wu and H. Lu, *Chem. Sci.*, 2024, **15**, 20440–20447.

8 M. Schulz, F. Balzer, D. Scheunemann, O. Arteaga, A. Lützen, S. C. J. Meskers and M. Schiek, *Adv. Funct. Mater.*, 2019, **29**, 1900684.

9 Y. Zhao, Y. Qiu, J. Feng, J. Zhao, G. Chen, H. Gao, Y. Zhao, L. Jiang and Y. Wu, *J. Am. Chem. Soc.*, 2021, **143**, 8437–8445.

10 L. Wang, Y. Xue, M. Cui, Y. Huang, H. Xu, C. Qin, J. Yang, H. Dai and M. Yuan, *Angew. Chem. - Int. Ed.*, 2020, **59**, 6442–6450.

11 S. You, P. Yu, T. Zhu, Q. Guan, J. Wu, H. Dai, H. Zhong, Z.-K. Zhu and J. Luo, *Mater. Horiz.*, 2023, **10**, 5307–5312.

12 X. Shang, L. Wan, L. Wang, F. Gao and H. Li, *J. Mater. Chem. C*, 2022, **10**, 2400–2410.

13 T. Liu, W. Shi, W. Tang, Z. Liu, B. C. Schroeder, O. Fenwick and M. J. Fuchter, *ACS Nano*, 2022, **16**, 2682–2689.

14 T. Zhu, H. Wu, C. Ji, X. Zhang, Y. Peng, Y. Yao, H. Ye, W. Weng, W. Lin and J. Luo, *Adv. Opt. Mater.*, 2022, **10**, 2200146.

15 W. Wu, X. Shang, Z. Xu, H. Ye, Y. Yao, X. Chen, M. Hong, J. Luo and L. Li, *Adv. Sci.*, 2023, **10**, 2206070.

16 X.-F. Luo, J. He, Y. Wang, H. Dai and Z.-G. Wu, *Chin. J. Struct. Chem.*, 2022, **41**, 70–79.

17 C. Chen, L. Gao, W. Gao, C. Ge, X. Du, Z. Li, Y. Yang, G. Niu and J. Tang, *Nat. Commun.*, 2019, **10**, 1927.

18 L. Mao, C. C. Stoumpos and M. G. Kanatzidis, *J. Am. Chem. Soc.*, 2019, **141**, 1171–1190.

19 J. Hu, L. Yan and W. You, *Adv. Mater.*, 2018, **30**, 1802041.

20 L. Cong and B.-B. Cui, *Sci. Sin. Chim.*, 2024, **54**, 1194–1211.

21 L. Yang, Y. Gao, Z. Wang, L. Yang and M. Shao, *Nat. Commun.*, 2025, **16**, 4161.

22 J. Hu, X. Wen, D. Yang, Y. Chen, Z. Liu and D. Li, *Nano Lett.*, 2024, **24**, 1001–1008.

23 J. Ahn, E. Lee, J. Tan, W. Yang, B. Kim and J. Moon, *Mater. Horiz.*, 2017, **4**, 851–856.

24 X. Dong, T. Chen, J. Liang, L. Wang, H. Wu, Z. Xu, J. Luo and L.-N. Li, *Chin. J. Struct. Chem.*, 2024, **43**, 100256.

25 Z. Zhu, T. Zhu, S. You, P. Yu, J. Wu, Y. Zeng, Y. Jiang, X. Liu, L. Li, C. Ji and J. Luo, *Adv. Sci.*, 2024, **11**, 2307593.

26 D. Li, W. Wu, S. Han, X. Liu, Y. Peng, X. Li, L. Li, M. Hong and J. Luo, *Chem. Sci.*, 2021, **12**, 3050–3054.

27 S. Ramakrishnan, Y. Dong, Y. Xie, J. L. Shelton, M. P. Hautzinger, D. Nguyen Minh, M. Taddei, X. Zhang, Y. Zhang, D. B. Mitzi, M. A. Haque, J. L. Blackburn, Q. Yu, M. C. Beard and J. M. Luther, *J. Am. Chem. Soc.*, 2025, **147**, 44457–44467.

28 G. Long, R. Sabatini, M. I. Saidaminov, G. Lakhwani, A. Rasmita, X. Liu, E. H. Sargent and W. Gao, *Nat. Rev. Mater.*, 2020, **5**, 423–439.

29 C. Ji, Y. Li, X. Liu, Y. Wang, T. Zhu, Q. Chen, L. Li, S. Wang and J. Luo, *Angew. Chem. - Int. Ed.*, 2021, **60**, 20970–20976.

30 R. Babu, J. E. Heger, T. Dutta, X. Hu, N. Pradhan, P. Müller-Buschbaum, S. Gómez-Graña and L. Polavarapu, *ACS Energy Lett.*, 2025, **10**, 5703–5721.

31 C. Coccia, M. Moroni and L. Malavasi, *Molecules*, 2023, **28**, 6166.

32 A. Dučinskas, M. Jung, Y.-R. Wang, J. V. Milić, D. Moia, M. Grätzel and J. Maier, *J. Mater. Chem. C*, 2024, **12**, 7909–7915.

33 J. M. Hoffman, X. Che, S. Sidhik, X. Li, I. Hadar, J.-C. Blancon, H. Yamaguchi, M. Kepenekian, C. Katan, J. Even, C. C. Stoumpos, A. D. Mohite and M. G. Kanatzidis, *J. Am. Chem. Soc.*, 2019, **141**, 10661–10676.

34 C. Asker, C. Pipitone, F. Ursi, K. Chen, A. G. Ricciardulli, E. S. Suena Galindez, S. Luong, P. Samorì, M. Reece, A. Martorana, F. Giannici and O. Fenwick, *J. Mater. Chem. A*, 2025, **13**, 26009–26018.

35 G. Long, C. Jiang, R. Sabatini, Z. Yang, M. Wei, L. N. Quan, Q. Liang, A. Rasmita, M. Askerka, G. Walters, X. Gong, J. Xing, X. Wen, R. Quintero-Bermudez, H. Yuan, G. Xing, X. R. Wang, D. Song, O. Voznyy, M. Zhang, S. Hoogland, W. Gao, Q. Xiong and E. H. Sargent, *Nat. Photonics*, 2018, **12**, 528–533.

36 Y.-H. Lee, G. M. Macam, R. A. B. Villaos, L.-Y. Feng, C.-H. Hsu, Z.-Q. Huang, D.-C. Wang, H. Lin and F.-C. Chuang, *J. Phys. Chem. C*, 2024, **128**, 17091–17097.

37 J. Son, S. Ma, Y.-K. Jung, J. Tan, G. Jang, H. Lee, C. U. Lee, J. Lee, S. Moon, W. Jeong, A. Walsh and J. Moon, *Nat. Commun.*, 2023, **14**, 3124.

38 S. An and P. Xing, *Chem. Soc. Rev.*, 2026, DOI:10.1039.D5CS00938C.

39 J. Son, G. Jang, S. Ma, H. Lee, C. U. Lee, S. Yang, J. Lee, S. Moon, W. Jeong, J. H. Park, J. Kim, D. H. Kim, J. Park and J. Moon, *Adv. Funct. Mater.*, 2025, **35**, 2413041.

40 Y. Fu, *Adv. Mater.*, 2022, **34**, 2108556.

41 D. Lin, L. Ma, W. Ni, C. Wang, F. Zhang, H. Dong, G. G. Gurzadyan and Z. Nie, *J. Mater. Chem. A*, 2020, **8**, 25402–25410.

42 J. Lu, W. Chen, C. Zhou, S. Yang, C. Wang, R. Wang, X. Wang, Z. Gan, B. Jia and X. Wen, *J. Mater. Chem. C*, 2021, **9**, 8966–8974.

43 X. Wang, X. Dong, H. Dong, Y. Zhou, C. Ran, L. Song, X. Liu, W. Xu, W. Huang and Z. Wu, *ACS Nano*, 2024, **18**, 26327−26337.

44 L. Tao, W. Tang, M. Yan, L. Ding, J. Wei, L. Wang, L. Li, L. Li, D. Yang and Y. Fang, *J. Mater. Chem. C*, 2023, **11**, 12392–12399.

45 J. Yu, M. Li, Y. Lv, B. Liao, G. Tan, J. Zou, X. Liu, Y. Han and L. Li, *Adv. Funct. Mater.*, 2025, **36**, e08904.

46 T.-M. Guo, F.-F. Gao, Y.-J. Gong, Z.-G. Li, F. Wei, W. Li and X.-H. Bu, *J. Am. Chem. Soc.*, 2023, **145**, 22475–22482.

47 P. Liu, N. Han, W. Wang, R. Ran, W. Zhou and Z. Shao, *Adv. Mater.*, 2021, **33**, 2002582.

48 Y. Lu, Y. Zhang, C.-Y. Yang, S. Revuelta, H. Qi, C. Huang, W. Jin, Z. Li, V. Vega-Mayoral, Y. Liu, X. Huang, D. Pohl, M. Položij, S. Zhou, E. Cánovas, T. Heine, S. Fabiano, X. Feng and R. Dong, *Nat. Commun.*, 2022, **13**, 7240.

49 H. S. Choi, J. Lin, G. Wang, W. P. D. Wong, I.-H. Park, F. Lin, J. Yin, K. Leng, J. Lin and K. P. Loh, *Science*, 2024, **384**, 60–66.

50 J. Ahn, S. Ma, J.-Y. Kim, J. Kyhm, W. Yang, J. A. Lim, N. A. Kotov and J. Moon, *J. Am. Chem. Soc.*, 2020, **142**, 4206–4212.

51 G. Long, C. Jiang, R. Sabatini, Z. Yang, M. Wei, L. N. Quan, Q. Liang, A. Rasmita, M. Askerka, G. Walters, X. Gong, J. Xing, X. Wen, R. Quintero-Bermudez, H. Yuan, G. Xing, X. R. Wang, D. Song, O. Voznyy, M. Zhang, S. Hoogland, W. Gao, Q. Xiong and E. H. Sargent, *Nat. Photonics*, 2018, **12**, 528–533.

52 Y. Mao, S. Guo, X. Huang, K. Bu, Z. Li, P. Q. H. Nguyen, G. Liu, Q. Hu, D. Zhang, Y. Fu, W. Yang and X. Lü, *J. Am. Chem. Soc.*, 2023, **145**, 23842–23848.

53 J. Son, S. Ma, Y.-K. Jung, J. Tan, G. Jang, H. Lee, C. U. Lee, J. Lee, S. Moon, W. Jeong, A. Walsh and J. Moon, *Nat. Commun.*, 2023, **14**, 3124.

54 J. Fu, T. Bian, J. Yin, M. Feng, Q. Xu, Y. Wang and T. C. Sum, *Nat. Commun.*, 2024, **15**, 4562.

55 A. G. Doyle and E. N. Jacobsen, *Chem. Rev.*, 2007, **107**, 5713–5743.

56 S. An and P. Xing, *Chem. Soc. Rev.*, 2026, **55**, 1461–1493.

57 Y. Liu, X. Zhang, X. Xu, J. Dai and Z. Quan, *Angew. Chem. Int. Ed.*, 2025, **64**, e202510579.

58 J. Tauc, in *Optical properties of solids*, eds S. Nudelman and S. S. Mitra, Springer US, Boston, MA, 1969, pp. 123–136.

59 S. Guo, W. Mihalyi-Koch, Y. Mao, X. Li, K. Bu, H. Hong, M. P. Hautzinger, H. Luo, D. Wang, J. Gu, Y. Zhang, D. Zhang, Q. Hu, Y. Ding, W. Yang, Y. Fu, S. Jin and X. Lü, *Nat Commun*, 2024, **15**, 3001.

60 J.-C. Blancon, H. Tsai, W. Nie, C. C. Stoumpos, L. Pedesseau, C. Katan, M. Kepenekian, C. M. M. Soe, K. Appavoo, M. Y. Sfeir, S. Tretiak, P. M. Ajayan, M. G. Kanatzidis, J. Even, J. J. Crochet and A. D. Mohite, *Science*, 2017, **355**, 1288–1292.

61 J. Tan, X. Jiang, D. Liu, Z.-K. Tang, E. V. Chulkov and A. S. Vasenko, *J. Phys. Chem. Lett.*, 2025, **16**, 7659–7665.

62 Y. Ma, J. Wang, Y. Liu, S. Han, Y. Li, Z. Xu, W. Guo, J. Luo, M. Hong and Z. Sun, *J. Mater. Chem. C*, 2021, **9**, 881–887.

63 S. Wang, X. Liu, L. Li, C. Ji, Z. Sun, Z. Wu, M. Hong and J. Luo, *J. Am. Chem. Soc.*, 2019, **141**, 7693–7697.

64 X. Li, F. Wu, Y. Yao, W. Wu, C. Ji, L. Li, Z. Sun, J. Luo and X. Liu, *J. Am. Chem. Soc.*, 2022, **144**, 14031–14036.

65 X. Zhang, W. Weng, L. Li, H. Wu, Y. Yao, Z. Wang, X. Liu, W. Lin and J. Luo, *Small*, 2021, **17**, 2102884.

66 Y. Zhao, X. Li, J. Feng, J. Zhao, Y. Guo, M. Yuan, G. Chen, H. Gao, L. Jiang and Y. Wu, *Giant*, 2022, **9**, 100086.

67 Y. Zhao, X. Yin, Z. Gu, M. Yuan, J. Ma, T. Li, L. Jiang, Y. Wu and Y. Song, *Adv. Funct. Mater.*, 2023, **33**, 2306199.

68 Z. Li, C. Ji, Y. Fan, T. Zhu, S. You, J. Wu, R. Li, Z.-K. Zhu, P. Yu, X. Kuang and J. Luo, *J. Am. Chem. Soc.*, 2023, **145**, 25134–25142.

69 Z. Liu, C. Zhang, X. Liu, A. Ren, Z. Zhou, C. Qiao, Y. Guan, Y. Fan, F. Hu and Y. S. Zhao, *Adv. Sci.*, 2021, **8**, 2102065.

View Article Online
DOI: 10.1039/D6SC00286B

Data availability statement

The data supporting this article have been included as part of the Supplementary Information.

Crystallographic data for (*R*-BrBA)$_2$EAPb$_2$Br$_7$ has been deposited at the CCDC under 2520919.

Crystallographic data for (*S*-BrBA)$_2$EA$_2$Pb$_2$Br$_7$ has been deposited at the CCDC under 2520920.

Crystallographic data for (*R*-BrBA)$_2$EA$_2$Pb$_3$Br$_{10}$ has been deposited at the CCDC under 2469041.

Crystallographic data for (*S*-BrBA)$_2$EA$_2$Pb$_3$Br$_{10}$ has been deposited at the CCDC under 2469438.